3 **Quantum mechanical modeling of hydrolysis and H$_2$O-exchange in Mg-, Ca-**

4 **and Ni-silicate clusters: Implications for dissolution mechanisms of olivine**

5 **minerals**

6

7 Christin P. Morrow,[1]*† Amanda A. Olsen,[2] and James D. Kubicki[3]

8

9 [1]*Department of Chemistry and Biochemistry, The University of Texas at Arlington, Arlington, TX*

10 *76019, USA*

11 [2]*School of Earth and Climate Sciences, The University of Maine, Orono, ME 04469, USA*

12 [3]*Department of Geosciences and the Earth & Environmental Systems Institute,*

13 *The Pennsylvania State University, University Park, PA 16802, USA*

14 **To whom correspondence should be addressed: morrow@uta.edu*

15 *†Permanent Address: Alcon Laboratories, 6201 South Freeway, Fort Worth, TX 76134*

16

17 **Abstract**

18 Barrier heights (BHs) for hydrolysis and H$_2$O exchange reactions at M–O–Si (M = Ni^{2+}, Mg^{2+},

19 and Ca^{2+}) linkages on olivine (M$_2$SiO$_4$) mineral surfaces were determined via DFT calculations.

20 BHs for hydrolysis of protonated Ni–O–Si, Mg–O–Si, and Ca–O–Si sites are 76, 54, and 27

21 kJ/mol, respectively, and are 69 and 24 kJ/mol for H$_2$O exchange reactions of protonated Mg–O–

22 Si and Ca–O–Si sites, respectively. Rate constants were calculated via classical transition state

23 theory (TST) using these BHs. For protonated Ni–O–Si, Mg–O–Si, and Ca–O–Si sites, these are

24 7.2 x 10^{-1}, 4.7 x 10^4, and 1.5 x 10^9 s^{-1} (pseudo-first order where [H$_2$O] is assumed to be

2

25   constant), respectively and for H_2O exchange at protonated Mg–O–Si and Ca–O–Si sites are 2.6

26   x 10^1 and 3.7 x 10^9 s^{-1} (pseudo-first order where $[H_2O]$ is assumed to be constant), respectively.

27   Approach of an H_2O molecule from the second hydration sphere toward a protonated Ni–O–Si

28   site leads to breakage of the Ni–O bond and subsequent release of Ni^{2+} to solution. For

29   protonated Mg–O–Si sites, however, H_2O exchange does not lead to rupture of the Mg–O bond

30   and would not be a step toward dissolution of the mineral. Potential energy surface (PES) scans

31   of H_2O exchange indicated formation of a hepta-coordinated Ca^{2+}, so neither H_2O exchange nor

32   hydrolysis of the Ca–O–Si linkage occurred in this case. Calculated rate constants are consistent

33   with experimental data for end-member composition olivine minerals where observed rates of

34   dissolution increase in the order $Ni^{2+} < Mg^{2+} < Ca^{2+}$.

35

36   **Keywords**

37   Dissolution, Silicate, Reaction Mechanism, Density Functional Theory (DFT), Quantum

38   Mechanical (QM), Rate Constant, H_2O Exchange, Hydrolysis

39

40   **Introduction**

41

42   Dissolution of minerals occurs via reaction of species from solution with sites on the

43   mineral surface, leading ultimately to breakdown of the original mineral structure and resulting

44   in release of elemental constituents to solution. This process is comprised of many elementary

45   reactions, including opening of the surface structure network, replacement of O atoms in the

46   metal surface polyhedra with H_2O molecules (Liu et al., 2006; Rosso and Rimstidt, 2000), and

47   surface site hydrolysis. This last class of reactions occurs when an H_3O^+ ion, H_2O molecule, or

3

48 OH^- ion from solution reacts with a metal site on the surface, breaking the M–O bond and

49 releasing a metal ion to solution.

50   The H_2O molecules, H_3O^+ ions, and OH^- ions from solution affect the dissolution rate

51 through two possible mechanisms. The effect of the H_3O^+ ion on the dissolution rate has been

52 described as proton-promoted dissolution (Furrer and Stumm, 1986; Stumm and Wollast, 1990),

53 where the dissolution rate of a mineral is observed to increase as a function of decreasing pH.

54 This is likely because H^+ ions adsorb to surface O atoms and weaken M–O and Si–O bonds. The

55 second proposed mechanism is known as ligand-promoted dissolution (Furrer and Stumm, 1986;

56 Ludwig et al., 1995; Stumm and Wollast, 1990), where the H_2O molecule and OH^- ion serve as

57 ligands bonding to the mineral surface. Their effect on the dissolution rate likely results from

58 weakening of M–O surface bonds via an increase in charge to the metal that is delivered by the

59 adsorbing ligand (Stumm and Wollast, 1990). At a given pH, there is a distribution of H^+, H_2O,

60 and OH^- species from solution reacting with surface sites, and thus proton- and ligand-promoted

61 pathways can both be active during dissolution (Furrer and Stumm, 1986).

62   Ligand-promoted dissolution is anomalous to ligand exchange reactions in solution

63 (Casey, 1991; Ludwig et al., 1995), and ligand exchange reactions, such as H_2O exchange, can

64 also occur on the mineral surface. In the case of silicate minerals, this process involves the

65 breaking and forming of M–O bonds at surface sites. Rates of H_2O exchange reactions around a

66 metal cation in solution correlate with the amount of energy required to break the M–O bond

67 (Casey, 1991; Casey and Rustad, 2007; Feitknecht and Hodler, 1969) as well as with the

68 dissolution rates of orthosilicate minerals (Casey, 1991; Casey and Ludwig, 1996; Casey and

69 Westrich, 1992; Westrich et al., 1993), a trend that is expected because both processes involve

70 breaking of M–O bonds – in the form of M–O, M–OH, or $M–OH_2$. As a result, the reaction

4

71 mechanisms for these two processes have been hypothesized to be fundamentally similar (Casey

72 and Westrich, 1992; Ludwig et al., 1995), and previous researchers have suggested that this

73 similarity enables a direct comparison between rates for ligand-promoted dissolution and H_2O

74 exchange reactions in solution (Ludwig et al., 1995). However, the amount of energy required to

75 break an M–O bond decreases across the following series: M–O > M–OH > M–OH$_2$. Therefore,

76 the rates of such reactions are not equal, and correlation of dissolution rates of orthosilicate

77 minerals with H_2O exchange rates (Casey and Westrich, 1992) may not mean that the

78 mechanisms are the same.

79 Both H_2O exchange reactions and ligand-promoted dissolution reactions in the form of

80 hydrolysis of M–O bonds occur at surface sites during dissolution of silicate minerals. What

81 remains to be seen is if these two phenomena are related and if the H_2O exchange rate of an

82 aqueous metal ion is an indicator of how dissolution proceeds for a mineral containing that

83 cation. There is no known chemical explanation (Casey, 1991) for correlation of H_2O exchange

84 reaction rates with the dissolution rates of orthosilicate minerals (Casey, 1991; Casey and

85 Ludwig, 1996; Casey and Westrich, 1992; Westrich et al., 1993). H_2O molecules are thought to

86 replace O atoms in mineral polyhedra during dissolution in acidic pH (Rosso and Rimstidt,

87 2000).

88 Although extensive experimental data exist (Casey, 1991; Casey and Westrich, 1992;

89 Davis et al., 2009; Pokrovsky and Schott, 2000; Rosso and Rimstidt, 2000), molecular

90 mechanisms of these surface reactions have yet to be described for divalent silicate minerals

91 using quantum mechanical techniques. The link between H_2O exchange reactions in solution and

92 dissolution of divalent silicate minerals has not been investigated from a molecular perspective.

93 Our hypothesis is that release of metals to solution occurs as a result of hydrolysis of M–O

5

94   linkages in the mineral network. One aim of this work is to test the hypothesis that H_2O

95   exchange reactions on the surface lead to M–O bond hydrolysis.

96   One approach for investigating the link between H_2O exchange reactions and dissolution

97   rates of minerals is to use quantum mechanical calculations that enable molecular-scale

98   investigation into reaction mechanisms. Previous work has studied the hydrolysis of sites on the

99   surface for aluminosilicates (Morrow et al., 2009; Xiao and Lasaga, 1994; Xiao and Lasaga,

100   1996), forsterite (Morrow et al., 2010), and quartz (Nangia and Garrison, 2008; 2009). These

101   studies analyzed experimental phenomena by using molecular clusters to simulate sites on the

102   mineral surface, and experimental observations were replicated (Morrow et al., 2009; 2010;

103   Nangia and Garrison, 2008). This approach allows the most fundamental aspect of a chemical

104   phenomenon to be investigated without interference of atoms that do not participate in the

105   reaction (Xiao and Lasaga, 1994). Therefore, molecular cluster investigations would allow for

106   analysis of H_2O exchange and hydrolysis reactions on the surface, enable description of the

107   reaction mechanisms, and provide insight into the link between H_2O exchange reaction rates for

108   metals in solution and dissolution rates for minerals containing these metals.

109   Questions remaining include whether H_2O exchange reactions are coupled with

110   dissolution, how H_2O exchange reactions affect dissolution, and if metal cations studied are

111   released from the mineral surface with similar mechanisms. Results from quantum mechanical

112   calculations employed in this work seek to answer these questions. Molecular clusters

113   representing protonated M–O–Si (M = Ni^{2+}, Mg^{2+}, and Ca^{2+}) sites on a mineral surface were

114   reacted with H_3O^+ ions to examine H_2O exchange and hydrolysis reactions and to determine

115   whether these processes are coupled for the end-member silicate minerals chosen. These

116   particular ions were chosen for this study because they represent orthosilicate minerals with

6

117   nearly the slowest through the fastest dissolution rates in experimental investigations (Casey,

118   1991; Casey and Rustad, 2007; Casey and Westrich, 1992). This work includes calculation of

119   barrier heights (BHs) and rate constants for these reactions, description of each reaction

120   mechanism, and comparison with experimental results.

121

122   **Computational Methods**

123   Reactions of H_2O with protonated M–O–Si (M = Ni^{2+}, Mg^{2+}, or Ca^{2+}) sites on olivine

124   surfaces were modeled with molecular clusters. The metal ion is hexa-coordinated via five H_2O

125   molecules and the M–O–Si linkage. Protonation is represented by an H^+ bonded to the O,

126   consistent with previous calculations of M–O bond breaking in large olivine systems (Liu et al.,

127   2006). The Si is bonded to three OH groups, representing bonds to the bulk crystal. Termination

128   via OH groups is supported by the observation that atoms farther than the next nearest neighbor

129   position participate minimally in bond breaking at the surface (Xiao and Lasaga, 1994). H_2O

130   exchange and hydrolysis reactions occurring at protonated M–O–Si surface sites are investigated

131   using these molecular cluster models. The presence of both the H^+ and the reacting H_2O

132   molecule represent the reaction of an H_3O^+ ion from solution with an M–O–Si site on the mineral

133   surface.

134   The reactions of these protonated clusters with an H_2O molecule are given in Equations 1

135   – 3. The protonated M–O–Si site is reacted with an H_2O molecule according to:

136     $[M(H_2O)_5(OH)Si(OH)_3]^{2+} + H_2O \rightarrow [M(H_2O)_6]^{2+} + Si(OH)_4$ (1)
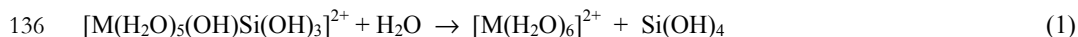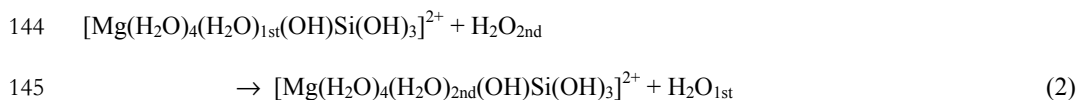
137   forming the hexaaqua metal(II) ion and silicic acid as products. Hydrolysis of Ni–O–Si, Mg–O–

138   Si, and Ca–O–Si sites eventually lead to these products in solution and on the mineral surface.

139   Formation of the hexaaqua Mg^{2+} ion and silicic acid form as products for hydrolysis of Mg–O–Si

7

140   sites is consistent with previous computational results for μ^3–O sites in large olivine clusters (Liu

141   et al., 2006).

142   In addition to hydrolysis of protonated sites, H_2O exchange at protonated Mg–O–Si and

143   Ca–O–Si sites is also investigated. For protonated Mg–O–Si sites, the reaction proceeds as:

144    $[Mg(H_2O)_4(H_2O)_{1st}(OH)Si(OH)_3]^{2+} + H_2O_{2nd}$

145        $\rightarrow [Mg(H_2O)_4(H_2O)_{2nd}(OH)Si(OH)_3]^{2+} + H_2O_{1st}$ (2)

146   where H_2O_{1st} is the H_2O molecule from the first hydration sphere that moves to the second, and

147   H_2O_{2nd} is the H_2O molecule from the second hydration sphere that moves to the first. A similar

148   approach was used to investigate H_2O exchange at a neutral Mg–O–Si site (Morrow et al., 2010).

149   For protonated Ca–O–Si sites, H_2O exchange is represented by the reaction:

150    $[Ca(H_2O)_5(OH)Si(OH)_3]^{2+} + H_2O \rightarrow [Ca(H_2O)_6(OH)Si(OH)_3]^{2+}$ (3)
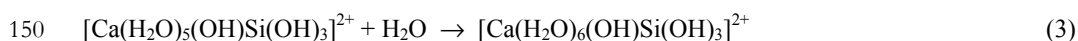
151   where instead of an exchange of H_2O molecules from the first and second hydration spheres, the

152   absorption of the second hydration sphere H_2O molecule into the primary hydration sphere forms

153   a hepta-coordinated Ca^{2+}.

154   The silicic acid product, $Si(OH)_4$, in Equation 1 represents a hydroxylated Si site that

155   remains on the surface after release of the metal to solution. Existence of charge is included in

156   the calculations by assigning a charge of +2 to the overall system. Thus, this charge is dispersed

157   throughout all the atoms in the system and is not solely located on the metal ion. However, for

158   clarity in this work as well as for ease in comparison with experimental data, the metals will each

159   be referred to in their ionic state.

160   Density functional theory (DFT) calculations have been shown to describe surface site

161   hydrolysis reactions successfully (Morrow et al., 2009; 2010; Nangia and Garrison, 2008; 2009;

162   Xiao and Lasaga, 1994; Xiao and Lasaga, 1996). In particular, B3LYP is used because of its

8

163   hybrid density functional nature, combining exchange-correlation (Becke, 1993a; 1993b; Lee et

164   al., 1988; Vosko et al., 1980), gradient correction (Becke, 1993a; 1993b), and a percentage of

165   Hartree-Fock exchange (Sousa et al., 2007). The 6-31G(d,p) basis set has been used to model

166   hydration of the Mg^{2+} ion (Adrian-Scotto et al., 2005) and here is used to investigate the

167   reactions in Equations 1 – 3. The absence of diffuse functions is advantageous for decreasing the

168   basis set superposition error (BSSE) on transition metal complexes (Rotzinger, 2005a); BSSE is

169   expected to be minimal as we report relative energy changes for molecular clusters, where the

170   intermolecular distances do not vary dramatically between configurations.

171   Molecular clusters representing protonated M–O–Si (M = Ni^{2+}, Mg^{2+}, and Ca^{2+}) sites

172   were constructed using experimental values for each M–O, Si–O, and O–H bond length and for

173   each M–O–H and Si–O–H bond angle. The M–O–Si bond angle was approximated from our

174   previous work (Morrow et al., 2010). Each molecular cluster was optimized with an H_2O

175   molecule in the second hydration sphere, and this optimized structure served as the starting

176   reactants for potential energy surface (PES) scans of H_2O exchange and hydrolysis reactions. For

177   H_2O exchange reactions, the distance between the H_2O in the second hydration sphere (H_2O_{2nd})

178   and the metal was constrained and decreased by 0.1 Å for 20 steps to represent approach of an

179   H_2O molecule from solution. This reaction coordinate was chosen because varying the distance

180   between the metal and the first hydration sphere H_2O molecule (H_2O_{1st}) underestimates bound

181   water lifetimes (Wang et al., 2007) and because the distance of H_2O_{2nd} from the metal is

182   considered fundamental to H_2O exchange (Casey et al., 2009). If the M–O bond did not break

183   during H_2O exchange, then a scan of the M–O distance was performed until it broke, and a

184   second scan of approach of H_2O_{2nd} was performed. Each of these scans was comprised of 20

9

185   steps, where each step was 0.1 Å. These two scans represent release of the metal ion to solution

186   and completion of the second hydration shell, respectively.

187   The structures with the lowest energy in the beginning and end of the scans were

188   optimized as reactant complex (RC) and product complex (PC), respectively, whereas the

189   structure with the highest energy was optimized as the transition state (TS). After optimization,

190   the dynamic stability of each calculated RC and PC was demonstrated by an absence of negative

191   frequencies; that is, each complex was at least in a local minimum. Possible TSs were identified

192   by the presence of one and only one negative (imaginary) frequency. For each reaction, this

193   negative frequency corresponded either to the forming of the $M–OH_2$ bond or to the breaking of

194   the M–O bond and thus the reaction coordinate between reactants and products. The energy of

195   each RC was set as zero, and the relative energies of the TS and PC were used to make the

196   energy profiles. The PES scans, geometry optimizations, and frequency calculations were

197   performed with Gaussian 03 (Frisch et al., 2004), and all images of the reaction mechanisms

198   were made with GaussView 4 (Dennington et al., 2007).

199   Once the RC and TS had been isolated for each reaction, the frequency output files were

200   used to calculate the rate constant according to the classical TST approximation and using

201   TheRate (Duncan et al., 1998; TheRate, 2006) according to the Arrhenius equation:

202    $k_T = AT^n e^{-(Ea/RT)}$ (4)

203   where A is the pre-exponential factor, T is the temperature in K, n is the exponential of the

204   temperature-dependence of A, E_a is the activation energy, and R is the gas constant (Duncan et

205   al., 1998; TheRate, 2006). However, the n exponent was set to zero to eliminate the temperature

206   dependence of A, and T was set to 298 K.

207

10

208   **Results and Discussion**

209   **Reaction Mechanisms and Energy Profiles for H$_2$O Exchange and Hydrolysis**

210   The PES scans present the energy of each configuration along the scan relative to the

211   energy of the RC, and the energy profiles represent the energy of the optimized TS and PC

212   species relative to the RC. The scans are presented in Figures 1a–5a along with the energy

213   profiles of the optimized RC, TS, and PC, whose structures appear in Figures 1b–5b and depict

214   the reaction mechanisms of the five reactions studied. The relevant bond lengths of the optimized

215   RC, TS, and PC as well as the bond angles of the TS for each reaction are given in Table 1, and

216   the BHs of all the reactions appear in Table 2.

217   **1. Protonated Ni–O–Si Sites.**

218   The PES scan and energy profile for reaction of a protonated Ni–O–Si site appear in

219   Figure 1a. The reaction mechanism comprised of the optimized RC, TS, and PC structures is

220   depicted in Figure 1b and shows concerted H$_2$O exchange and Ni–O bond break. In the RC,

221   H$_2$O$_{2nd}$ is H-bonded to the H on the O in the Ni–O–Si linkage as well as to an equatorial H$_2$O

222   molecule. As H$_2$O$_{2nd}$ approaches Ni^{2+}, the equatorial H$_2$O molecules begin to rearrange to

223   accommodate the incoming H$_2$O molecule, as shown in the TS. The negative frequency

224   corresponds to formation of the Ni–OH$_2$ bond. As a result, approach of H$_2$O leads to breaking of

225   the Ni–O bond, and this is evident in the PC by the presence of the hexaaqua Ni^{2+} ion and the

226   absence of the Ni–O bond, leaving silicic acid as the second product. The barrier height for this

227   reaction is 76 kJ/mol.

228   Distances between the incoming H$_2$O molecule and the metal ion as well as between the

229   metal ion and the O atom indicate the degree to which the associated bonds are forming and

230   breaking, respectively, within these molecular clusters and also provide insight into how the

                                                                                            11

231 constituents in the RC and PC resemble their counterparts on the mineral surface and in solution.

232 The distances between Ni^{2+} and H_2O_{2nd} and Ni^{2+} and O are listed in Table 1 for the optimized

233 RC, TS, and PC. In the RC, the Ni–H_2O distance is 3.81 Å, and the Ni–O distance is 2.10 Å. For

234 the TS, the Ni–H_2O distance has decreased to 2.51 Å, while the Ni–O distance has increased to

235 2.14 Å. The final Ni–H_2O and Ni–O distances in the PC are 2.11 Å and 4.02 Å, respectively.

236   The bond angles surrounding Ni^{2+} in the TS are also included in Table 1. The bond

237 angles surrounding Ni^{2+} in the TS are listed starting from the equatorial H_2O molecule in the

238 right foreground of Figure 1b and continue counter-clockwise. The O–Ni–H_2O_{eq} angles are 109°,

239 109°, 83°, and 83°, while the H_2O_{ax}–Ni–H_2O_{eq} bond angles are 82°, 87°, 86°, and 78°. The O–

240 Ni–H_2O_{eq} angles closest to the approaching second hydration sphere H_2O molecule are increased

241 from the expected 90° for an octahedral complex, and these groups are rearranged as a result of

242 the incoming H_2O molecule.

243   Approach of a second hydration sphere H_2O molecule toward a protonated Ni–O–Si site

244 leads to release of Ni^{2+}, in the form of $Ni(H_2O)_6^{2+}$, to solution. The PES scan and mechanism for

245 this reaction indicate that H_2O exchange leads to Ni–O bond break. Thus for protonated Ni–O–Si

246 sites, the H_2O exchange and hydrolysis reactions are one and the same.

247   **2. Protonated Mg–O–Si Sites.**

248   The H_2O exchange reaction for a protonated Mg–O–Si site is shown in Figure 2. A PES

249 scan of the constrained distance between Mg^{2+} and H_2O_{2nd} as the reaction coordinate and the

250 energy profile of the optimized RC, TS, and PC appear in Figure 2a. The structures of the

251 optimized RC, TS, and PC are shown in Figure 2b. As the incoming H_2O approaches Mg^{2+}, the

252 equatorial H_2O molecules begin to rearrange to enable the exchange. The TS is characterized by

253 elongated bonds to the first hydration shell H_2O molecules and to O. Also in the TS, H_2O_{1st}

12

254   (green circle) begins to leave the first hydration shell, whereas H_2O_{2nd} (blue circle) enters the

255   first hydration shell. For this reaction, the negative frequency corresponds to a concerted

256   interaction of the approaching H_2O molecule with the H-bonding network of the equatorial H_2O

257   molecules. In the PC, the Mg–O bond is intact, and H_2O_{1st} has been replaced by H_2O_{2nd} as shown

258   in Figure 2b. The barrier height for this reaction is 69 kJ/mol.

259   The distances between Mg^{2+} and H_2O_{2nd} as well as Mg^{2+} and H_2O_{1st} are listed in Table 1

260   for the optimized RC, TS, and PC in the H_2O exchange reaction for the protonated Mg–O–Si

261   site. In the RC, the Mg–H_2O_{2nd} distance is 3.85 Å, and the Mg–H_2O_{1st} distance is 2.10 Å. In the

262   TS, the Mg–H_2O_{2nd} distance is 2.20 Å, shorter than the Mg–H_2O_{1st} distance of 2.26 Å. The final

263   Mg–H_2O_{2nd} distance is 2.10 Å, and the final Mg–H_2O_{1st} distance is 3.84 Å.

264   The bond angles surrounding the Mg^{2+} in the TS are listed in Table 1 using either O or

265   the axial H_2O as anchors, starting from the equatorial H_2O molecule in the right foreground of

266   Figure 2b and continuing counter-clockwise. The O–Mg–H_2O_{eq} bond angles are 106°, 107°, 82°,

267   and 80°, while the H_2O_{ax}–Mg–H_2O_{eq} angles are 77°, 83°, 89°, and 85°. As with the reaction for

268   the protonated Ni–O–Si site, the O–Mg–H_2O_{eq} bond angles show that the equatorial H_2O

269   molecules are widening to accommodate the incoming H_2O molecule.

270   Because the stepwise approach of H_2O did not lead to the breaking of the Mg–O bond,

271   the possibility of Mg–O bond lengthening as the cause of bond break was examined. The

272   hydrolysis of a protonated Mg–O–Si site appears in Figure 3. The PES scan is comprised of two

273   steps: the breaking of the Mg–O bond and the absorption of the incoming H_2O molecule by

274   Mg^{2+}. The reaction coordinate for the first step is the lengthening of the Mg–O bond, and in the

275   second step, it is the decreasing of Mg–H_2O distance for H_2O_{2nd}. The optimized RC, TS, and PC

276   structures comprise the energy profile in Figure 3a and are shown as the reaction mechanism in

13

277   Figure 3b. The RC in Figure 3b shows H_2O_{2nd} H-bonded to the H^+ on O and an equatorial H_2O

278   molecule, in much the same manner as for the protonated Ni–O–Si site. The Mg–O bond is

279   lengthened until it breaks in the TS, where the negative frequency here corresponds to the

280   breaking of the Mg–O bond, but H_2O_{2nd} is not yet absorbed by Mg^{2+} in the TS. H_2O_{2nd}

281   approaches the penta-coordinated Mg^{2+} between the TS and PC and is absorbed in the PC, and

282   thus, the PC is comprised of the hexaaqua Mg^{2+} ion and silicic acid. The BH for this reaction is

283   54 kJ/mol.

284   The distances between Mg^{2+} and H_2O_{2nd} as well as between Mg^{2+} and O are listed in

285   Table 1. In the RC, H_2O_{2nd} is 3.85 Å from Mg^{2+}, whereas the Mg–O distance is 2.14 Å. In the

286   TS, the Mg–H_2O distance has increased to 4.28 Å, and the Mg–O distance has increased to 3.74

287   Å. The Mg–H_2O_{2nd} distance increases in the TS to allow for rearrangement of equatorial H_2O

288   molecules around Mg^{2+}. The final distances for Mg–H_2O_{2nd} and Mg–O are 2.09 Å and 4.11 Å,

289   respectively.

290   The bond angles around Mg^{2+} in the TS are also included in Table 1. The bond angles

291   surrounding Mg^{2+} in the TS are listed using either O or the axial H_2O as anchors, start from the

292   equatorial H_2O molecule in the right foreground of Figure 3b, and continue counter-clockwise.

293   The O–Mg–H_2O_{eq} are 70°, 105°, 72°, and 70°, whereas the H_2O_{ax}–Mg–H_2O_{eq} bond angles are

294   112°, 91°, 109°, and 93°. These show that the geometry around Mg^{2+} is approaching an

295   octahedral configuration (*i. e.* O–Mg–O angles = 90°), which facilitates absorption of H_2O_{2nd}.

296   For protonated Mg–O–Si sites, H_2O exchange and hydrolysis reactions are de-coupled.

297   Approach of an H_2O molecule causes an H_2O from the first hydration sphere to be replaced by

298   one from the second, such that the Mg–O bond break is not a result of the approach of the H_2O

14

299   molecule. Instead, breaking of the Mg–O bond occurs as a result of lengthening of the Mg–O

300   bond.

301   **3. Protonated Ca–O–Si Sites.**

302   An examination of H_2O exchange for Ca–O–Si sites was performed as well. In this

303   reaction, H_2O_{2nd} is absorbed by Ca^{2+} and leads to formation of a hepta-coordinated Ca^{2+}. Thus, a

304   true H_2O exchange reaction does not occur for this site in these calculations; instead an H_2O

305   addition occurs. The PES scan is performed where the incoming H_2O molecule approaches Ca^{2+}

306   (Figure 4a). The energies of the optimized RC, TS, and PC are shown in Figure 4a and the

307   structures in Figure 4b. In the RC, H_2O_{2nd} is H-bonded to the H on O and an equatorial H_2O

308   molecule. As H_2O_{2nd} approaches Ca^{2+}, the equatorial H_2O molecules begin to rearrange to

309   accommodate the incoming H_2O molecule as shown in the TS, and the negative frequency

310   corresponds to formation of this $Ca–OH_2$ bond. However, unlike both the protonated Ni–O–Si

311   and Mg–O–Si sites, the H_2O molecule is absorbed to form a hepta-coordinated Ca^{2+}, and thus,

312   the sole product is this newly-formed calcium silicate cluster. The BH for this reaction is 24

313   kJ/mol.

314   The $Ca–H_2O_{2nd}$ and Ca–O distances appear in Table 1. In the RC, the $Ca–H_2O_{2nd}$ distance

315   is 4.09 Å, and the Ca–O distance is 2.46 Å. The $Ca–H_2O_{2nd}$ distance decreases to 2.99 Å in the

316   TS, while the Ca–O distance remains nearly constant and is 2.45 Å. In the PC, the $Ca–H_2O_{2nd}$

317   and Ca–O distances are nearly equal at 2.51 Å and 2.52 Å, respectively.

318   The bond angles surrounding Ca^{2+} in the TS are also included in Table 1. The bond

319   angles surrounding Ca^{2+} in the TS are listed using either the protonated O or the axial H_2O as

320   anchors, start from the equatorial H_2O molecule in the right foreground of Figure 4b, and

321   continue counter-clockwise. The $O–Ca–H_2O_{eq}$ bond angles are 122°, 100°, 75°, and 77°, whereas

15

322 the H_2O_{ax}–Ca–H_2O_{eq} bond angles are 84°, 93°, 84°, and 77°. These angles show that the

323 octahedral geometry around Ca^{2+} is distorting, enabling accommodation of the seventh bonded

324 group.

325   Because stepwise approach of H_2O_{2nd} did not lead to breaking of the Ca–O bond, the Ca–

326 O bond was lengthened as a possible cause for bond break. The hydrolysis of a protonated Ca–

327 O–Si site appears in Figure 5. The initial PES scan appears in Figure 5a and is indicated by

328 closed blue triangles and a blue line. The first step in this scan consists of the lengthening and

329 subsequent breaking of the Ca–O bond, whereas the second step is the addition of the H_2O

330 molecule to the first hydration sphere. This first attempt to determine the BH for hydrolysis of a

331 protonated Ca–O–Si site led to a barrier height of ~70 kJ/mol, which is higher than the expected

332 value of 25–30 kJ/mol (Tsutsui et al., 1997).

333   Therefore, products from this scan were optimized and used to perform a scan of this

334 reaction in the reverse direction, which appears as open blue triangles in Figure 5a. This strategy

335 is employed to determine whether the chosen reaction coordinate is an accurate representation of

336 the progress of this reaction (Foresman and Frisch, 1996). The TS from this scan was 27 kJ/mol

337 higher in energy than the hexa-coordinated RC from the first scan, making it a representative

338 structure of the overall mechanism. However, the scan in the reverse direction led to the hepta-

339 coordinated Ca-silicate cluster shown as the PC in Figure 4b. The points in the PES scan for the

340 reverse direction represent a coarser scan to identify the structure of the TS where the Ca–O

341 bond breaks through a lower energy process. Thus, the energy profile in Figure 5a and the

342 reaction mechanism in Figure 5b consist of the hexa-coordinated RC, the TS from the reverse

343 scan, and the hexa-coordinated PC.

16

344   In the reaction mechanism in Figure 5b, H_2O_{2nd} is H-bonded to the H on the O and an

345   equatorial H_2O molecule. The Ca–O bond is lengthened and eventually breaks in the TS, and

346   H_2O_{2nd} is already absorbed. The negative frequency in the TS for this reaction corresponds to the

347   breaking of the Ca–O bond. The PC is characterized by an increase in the Ca–O distance, given

348   below, and a fully formed octahedral geometry around Ca^{2+}.

349   The distances between Ca^{2+} and H_2O_{2nd} as well as between Ca^{2+} and O appear in Table 1.

350   In the RC, the Ca–H_2O_{2nd} distance is 4.09 Å, and the Ca–O distance is 2.46 Å. The Ca–H_2O_{2nd}

351   distance decreases to 2.44 Å in the TS, and the Ca–O distance increases to 3.04 Å. The final Ca–

352   H_2O_{2nd} and Ca–O distances are 2.39 Å and 4.34 Å, respectively, in the PC.

353   The bond angles surrounding Ca^{2+} in the TS are listed in Table 1 using either the H_2O in

354   the foreground or the H_2O in the background of Figure 5b as anchors, start from the equatorial

355   H_2O molecule in the right foreground of Figure 5b, and continue counter-clockwise. This method

356   of analysis is used as opposed to the remaining bond angles given in Table 1 because here the

357   incoming H_2O molecule has already been absorbed in the TS. The H_2O_{fore}–Ca–H_2O_{eq} bond

358   angles are 83°, 92°, 79°, and 87°, whereas the H_2O_{back}–Ca–H_2O_{eq} bond angles are 124°, 93°, 75°,

359   and 92°. These angles show that the octahedral geometry around Ca^{2+} is nearly complete in the

360   TS.

361   The formation of a hepta-coordinated Ca^{2+} in the H_2O exchange reaction for a protonated

362   Ca–O–Si site warrants additional comment. The first hydration shell of Ca^{2+} has been shown to

363   vary from six to eight (Ikeda et al., 2007; Jalilehvand et al., 2001; Schwenk et al., 2001).

364   However, these simulations (Ikeda et al., 2007; Jalilehvand et al., 2001; Schwenk et al., 2001)

365   and experiments (Jalilehvand et al., 2001) were performed for the solution phase and not for the

366   solid state. Molecular clusters used in this work are intended to represent individual sites on a

17

367   mineral surface, which would be surrounded by many other surface sites. Therefore, formation of

368   a hepta-coordinated Ca^{2+} would be unlikely throughout the mineral surface because of steric

369   crowding but could be possible at more exposed sites like defects or edges. As such, this

370   increased coordination would facilitate easier release of Ca^{2+} ions, similar to the model proposed

371   by Rosso and Rimstidt (2000).

372   Comparison of H_2O exchange and hydrolysis for protonated Ca–O–Si sites leads to a

373   third reaction scheme where these two reactions are coupled. Formation of a hepta-coordinated

374   Ca^{2+} indicates that breaking of the Ca–O bond is not affected by approach of an H_2O molecule

375   from the second hydration sphere. This is further reinforced by the elusive nature of the PES

376   scan for hydrolysis of a protonated Ca–O–Si site and is manifested by the similarity of the BHs

377   and rate constants, given in the next section, for these reactions. The ability of Ca^{2+} to

378   accommodate a large number of groups (Jalilehvand et al., 2001) is what contributes to this

379   complication. However, this elusive behavior likely shows that a specific degree of freedom

380   affects which path is chosen.

381   **Rate Constants**

382   The pre-exponential factors and rate constants for the reactions in Equations 1–3 are

383   given in Table 3, and the rate constants were calculated using Equation 4. The rate constants

384   follow the opposite trend as the barrier heights outlined above, as is expected. There are two rate

385   constants for the protonated Mg–O–Si site corresponding to H_2O exchange and hydrolysis

386   reactions, and these rate constants indicate that hydrolysis would proceed more rapidly than H_2O

387   exchange. Similarly for protonated Ca–O–Si sites, the two rate constants are for formation of the

388   hepta-coordinated complex and hydrolysis of this site, where the rate constant of the former is

389   slightly higher than that of the latter. The log of these rate constants are plotted against the log of

18

390   rate constants for H_2O exchange around each corresponding metal ion (Casey and Westrich,

391   1992; Helm and Merbach, 1999) in Figure 6, similar to the analysis of previous researchers

392   (Casey and Westrich, 1992), and the uncertainty of each datum is roughly the size of the point in

393   the figure (*i. e.* one order of magnitude). The trend is such that the rate constant for the reactions

394   of each metal increases with the rate constant for H_2O exchange around the corresponding metal

395   ion.

Overall Trends and Comparison to Experiment

397   The data in Figure 6 replicate the experimental trend for these systems (Casey and

398   Westrich, 1992), where rates for end-member orthosilicate dissolution increase in the order Ni^{2+}

399    $< Mg^{2+} < Ca^{2+}$. Reaction mechanisms described in this work provide additional insight into the

400   relation of M–O bond energies, H_2O exchange rates, and mineral dissolution. The rate constant

401   for hydrolysis of a protonated surface site increases as the amount of energy required to break the

402   M–O bond decreases, as has been discussed (Casey, 1991; Casey and Rustad, 2007; Stumm and

403   Wollast, 1990). However, what is most intriguing from these calculations is that H_2O exchange

404   and hydrolysis reactions are not always intimately related at sites within the clusters, and for

405   some minerals, these phenomena are exclusive for Mg–O–Si and Ca–O–Si linkages. The data in

406   Figure 6 also show that H_2O exchange and hydrolysis rate constants are not equal and are likely

407   two reactions occurring within the overall dissolution process.

408   Although the data in Figure 6 replicate the experimental trend (Casey and Westrich,

409   1992), the values are different. Experimental dissolution rates extend across ~5 orders of

410   magnitude, whereas those in Figure 6 differ by ~9 orders of magnitude. There are two possible

411   explanations for this. The higher rate constants calculated here indicate that experimental

412   phenomena contribute to the rate and somehow affect metal release from the surface. Secondly,

19

413   the experiments on olivine minerals are at pH = 2 (Casey and Westrich, 1992), and although the

414   clusters shown here represent protonated sites on the surface, the phenomena are different

415   because mineral surfaces contain a distribution of sites in protonated, neutral, and deprotonated

416   states at each pH.

417   The results presented offer a molecular-scale insight into the link between H_2O exchange

418   and the release of metal ions to solution during mineral dissolution. Comparison of experimental

419   and calculated energies for H_2O exchange around $Ni(H_2O)_6^{2+}$, $Mg(H_2O)_6^{2+}$, and $Ca(H_2O)_6^{2+}$ ions

420   (Bechtold et al., 1978; Bleuzen et al., 1997; Kang et al., 1991; Neely and Connick, 1970;

421   Rotzinger, 1996; Tsutsui et al., 1997) as well as experimental rate constants given on the x-axis

422   of Figure 6 shows that there are differences between H_2O exchange reactions for these ions and

423   for the reactions described in this work. The presence of a silicic acid group instead of a sixth

424   H_2O molecule around the metal ion is likely responsible for the difference in the H_2O exchange

425   rate constants and the rate constants measured here (Helm and Merbach, 2005; Richens, 2005).

426   There are two types of reactions in this regard. The first is where the silicic acid does not

427   participate in the reaction; that is, the M–O bond remains intact. For both the H_2O exchange

428   reaction at the protonated Mg–O–Si site and the formation of the hepta-coordinated Ca^{2+}, this

429   silicic acid group affects the rate constant. The H_2O exchange rate constant for $Mg(H_2O)_6^{2+}$ is

430   higher than the rate constant for the reaction in Equation 2, and this shows that the silicic acid

431   kinetically limits the H_2O exchange reaction at a protonated Mg–O–Si site. For the protonated

432   Ca–O–Si site, on the other hand, the rate constant for the formation of the hepta-coordinated

433   Ca^{2+} in the silicate molecular cluster is an order of magnitude larger than that for H_2O exchange

434   on $Ca(H_2O)_6^{2+}$. In this case, the silicic acid group is kinetically enhancing H_2O exchange.

20

435   For hydrolysis of protonated Ni–O–Si, Mg–O–Si, and Ca–O–Si sites, the silicic acid

436   group now participates in the reaction; that is, the breaking of the M–O bond occurs. In these

437   three reactions, the effect of the silicic acid group can also be examined. During hydrolysis,

438   H_2O_{2nd} replaces the silicic acid group, and as a result, the rate constants for these reactions are

439   different than those for H_2O exchange reactions for $Ni(H_2O)_6^{2+}$, $Mg(H_2O)_6^{2+}$, and $Ca(H_2O)_6^{2+}$.

440   For both protonated Ni–O–Si and Mg–O–Si sites, hydrolysis reactions have smaller rate

441   constants than those for H_2O exchange reactions, whereas for protonated Ca–O–Si sites, rate

442   constants for hydrolysis is larger than that for H_2O exchange around $Ca(H_2O)_6^{2+}$. These results

443   suggest that the correlation of dissolution for end-member orthosilicate minerals with rate

444   constants of H_2O exchange (Casey and Westrich, 1992) is coincidental (and likely based on

445   similar relative bond strengths between each metal and either O atoms, OH^-, or H_2O) and not an

446   indication that H_2O exchange is the mechanism of dissolution.

447   However, both mineral dissolution and H_2O exchange rely on breaking M–O bonds and

448   the forming $M–OH_2$ bonds, and thus, the link between M–O bond energy and mineral dissolution

449   rates (Casey and Rustad, 2007) is also not surprising (Stumm and Wollast, 1990). Furthermore,

450   this connection may show that the bonding environment around the metal ion is similar in the

451   mineral as in the $M(H_2O)_6^{2+}$ ion, particularly for transition metals (Helm and Merbach, 2002).

452   Moreover, the occupancy of the d orbitals on Ni^{2+} is the same for both the complexes shown and

453    $Ni(H_2O)_6^{2+}$, and the rates of H_2O exchange reactions are known to scale with d orbital occupancy

454   for transition metals (Ducommun et al., 1980; Helm and Merbach, 2002; Richens, 2005;

455   Rotzinger, 2005b). The rate constants calculated also increase with the ionic size of the metal

456   ion, as has been observed in other studies (Casey, 1991; Casey and Westrich, 1992; Helm and

457   Merbach, 2002; 2005; Richens, 2005).

21

458   Hydrolysis of protonated Mg–O–Si sites proceeds through a dissociative (D) mechanism.

459   This reaction can be characterized as such because of the decrease in coordination arising from

460   the breaking of the Mg–O bond (Langford and Gray, 1966) and because the Mg–O distance in

461   the TS is > 1.0 Å longer than it was in the RC (Rotzinger, 1997). This dissociative type

462   mechanism is expected for protonated Mg–O–Si sites based on known mechanisms for H_2O

463   exchange around this ion (Helm and Merbach, 2002; 2005; Richens, 2005), and the primary

464   reason for this expectation is the ionic radius of Mg^{2+} (Ducommun et al., 1980; Richens, 2005).

465   On the other hand, hydrolysis of protonated Ni–O–Si sites and H_2O exchange at

466   protonated Mg–O–Si sites are in contrast to expectations (Ducommun et al., 1980; Helm and

467   Merbach, 2002; 2005; Richens, 2005; Rotzinger, 1996; 1997). These two reactions appear to

468   proceed through an associative interchange (I_a) mechanism for three reasons. First, negative

469   frequencies correspond to M–OH_2 bond formation or concerted motion within the H-bonding

470   network. Second, the Ni–O and Mg–H_2O_{1st} bonds have not lengthened significantly, < 1.0 Å, in

471   the TS, and third, the bond angles of the octahedron are distorted in the TS. The Ni–O–Si sites

472   are expected to react via dissociative mechanisms because of the population of the d orbitals

473   (Ducommun et al., 1980; Helm and Merbach, 2002; Richens, 2005; Rotzinger, 2005b) and

474   because approach of the seventh molecule toward the face of the octahedron is electrostatically

475   unfavorable (Ducommun et al., 1980; Richens, 2005). Also, the small size of the Mg^{2+} ion

476   prevents the incorporation of a seventh group (Ducommun et al., 1980; Richens, 2005).

477   However, a review of ligand exchange mechanisms showed that Ni^{2+} can react via D or

478   associative (A) mechanisms, depending upon the ligands present (Helm and Merbach, 2005). In

479   addition, two previous studies (Rotzinger, 1996; 1997) investigated H_2O exchange mechanisms

480   around $Ni(H_2O)_6^{2+}$ via ab initio calculations. A Hartree-Fock (HF) computational approach was

22

481   employed because a DFT approach was not possible for transition metals at that time (Rotzinger,

482   1996). A TS for the associative, A or I_a, mechanisms (Rotzinger, 1996), was not isolated. The

483   TSs presented were square pyramidal in geometry (Rotzinger, 1996; 1997), and the hepta-

484   coordinated TS and intermediate had two negative frequencies (Rotzinger, 1996). The author

485   posed the possibility that these results arose as a result of the method used (Rotzinger, 1996).

486   These discrepancies in the literature demonstrate that additional investigations are needed.

487   The mechanism for the formation of hepta-coordinated Ca^{2+} can be classified as

488   associative (A) because absorption of the incoming H_2O molecule forms a hepta-coordinated

489   complex without negative frequencies. This is not surprising as an associative mechanism is

490   expected for Ca^{2+} because of its ionic size (Richens, 2005). One could suggest that perhaps the

491   development of a hepta-coordinated Ca^{2+} arises because of the employment of a computational

492   approach via molecular clusters. In fact, DFT methods have been shown to prefer decreased

493   coordination numbers for metal ions and thus dissociative mechanisms over associative ones

494   (Rotzinger, 2005b). Therefore, the presence of a hepta-coordinated Ca^{2+} ion in this work is

495   consistent with previous results (Ikeda et al., 2007; Jalilehvand et al., 2001; Schwenk et al.,

496   2001) and demonstrates this result is not an artifact of gas-phase clusters analyzed by DFT

497   methods.

498   The hydrolysis of Ca–O–Si sites is difficult to classify. On one hand, the TS is

499   characterized by the breaking of the Ca–O bond, which is indicative of a dissociative interchange

500   (I_d) mechanism (Helm and Merbach, 2005; Richens, 2005; Rotzinger, 2005b). However, the

501   coordination number of Ca^{2+} has not decreased. On the other hand, the Ca–OH_2 bond is nearly

502   fully-formed in the TS, and thus an A mechanism would seem to be an appropriate classification.

503   In this case, the TS would be marked by a negative frequency corresponding to the formation of

23

504   the Ca–OH$_2$ bond, which it is not. Thus, the hydrolysis reaction Ca–O–Si sites does not seem to

505   fit into any of the classifications of Langford and Gray (1966), and this reinforces the

506   observation that Ca^{2+} can react via *A* or *D* mechanisms (Akesson et al., 1994). Additional

507   analyses are necessary to further elucidate a straightforward description of the PES for

508   hydrolysis at protonated Ca–O–Si surface sites.

509

510   **Implications**

511   The correlation between H$_2$O exchange reaction rates and dissolution of end-member

512   silicate minerals is not surprising given their mutual dependence upon M–O bond breakage and

513   formation. However, the results presented here are unique in that they show differences in the

514   mechanisms through which various metal sites react. Minerals containing these metals cannot be

515   assumed to dissolve in the same fashion or according to the same rate model as one another. As

516   such, the work presented here begs the question, "Does each metal site react according to its own

517   mechanism?" Further study in this field is necessary to answer this question.

518   In addition to dissolution of minerals, the results represented here also have implications

519   to the dissolution and design of industrial materials. Glasses intended for nuclear waste storage,

520   for example, may remain structurally intact longer if the glass network includes transition metals

521   over alkaline metals, given the larger BH and smaller rate constant calculated here. On the

522   contrary, materials intended to promote CO$_2$ storage through formation of a geologic phase hinge

523   upon release of metals, such as Mg^{2+} and Ca^{2+}, and therefore, in these applications, rapidity of

524   metal ion release is desirable. As such, intended use of the material requires knowledge of

525   dissolution mechanisms like those proposed here to enable efficient design of these materials.

526

24

527

539

References Cited

541 Adrian-Scotto, M., Mallet, G., and Vasilescu, D. (2005) Hydration of Mg++: a quantum DFT
542   and ab initio HF study. Journal of Molecular Structure-Theochem, 728(1-3), 231-242.

543 Akesson, R., Pettersson, L.G.M., Sandstrom, M., and Wahlgren, U. (1994) Theoretical-study on
544   water-exchange reactions of the divalent and trivalent metal ions of the first transition
545   period. Journal of the American Chemical Society, 116(19), 8705-8713.

546 Bechtold, D.B., Liu, G., Dodgen, H.W., and Hunt, J.P. (1978) O-17 Nuclear magnetic-resonance
547   study of aquo nickel(II) sulfate system. Journal of Physical Chemistry, 82(3), 333-337.

548 Becke, A.D. (1993a) Density-functional thermochemistry. III. The role of exact exchange.
549   Journal of Chemical Physics, 98(7), 5648-5652.

25

550   -. (1993b) A new mixing of Hartree-Fock and local density-functional theories. Journal of

551   Chemical Physics, 98(2), 1372-1377.

552   Bleuzen, A., Pittet, P.A., Helm, L., and Merbach, A.E. (1997) Water exchange on magnesium(II)

553   in aqueous solution: a variable temperature and pressure O-17 NMR study. Magnetic

554   Resonance in Chemistry, 35(11), 765-773.

555   Casey, W.H. (1991) On the relative dissolution rates of some oxide and orthosilicate minerals.

556   Journal of Colloid and Interface Science, 146(2), 586-589.

557   Casey, W.H., and Ludwig, C. (1996) The mechanism of dissolution of oxide minerals. Nature,

558   381(6582), 506-509.

559   Casey, W.H., and Rustad, J.R. (2007) Reaction dynamics, molecular clusters, and aqueous

560   geochemistry. Annual Review of Earth and Planetary Sciences, 35, 21-46.

561   Casey, W.H., Rustad, J.R., and Spiccia, L. (2009) Minerals as molecules-use of aqueous oxide

562   and hydroxide clusters to understand geochemical reactions. Chemistry-A European

563   Journal, 15(18), 4496-4515.

564   Casey, W.H., and Westrich, H.R. (1992) Control of dissolution rates of orthosilicate minerals by

565   divalent metal oxygen bonds. Nature, 355(6356), 157-159.

566   Davis, M.C., Brouwer, W.J., Wesolowski, D.J., Anovitz, L.M., Lipton, A.S., and Mueller, K.T.

567   (2009) Magnesium silicate dissolution investigated by Si-29 MAS, H-1-Si-29 CPMAS,

568   Mg-25 QCPMG, and H-1-Mg-25 CP QCPMG NMR. Physical Chemistry Chemical

569   Physics, 11(32), 7013-7021.

570   Dennington, R., II, Keith, T., and Millam, J. (2007) GaussView, Version 4.1. Semichem, Inc.,

571   Shawnee Mission, KS.

26

572   Ducommun, Y., Newman, K.E., and Merbach, A.E. (1980) High-pressure NMR kinetics .II.

573   High-pressure O-17 NMR evidence for a gradual mechanistic changeover from Ia to Id

574   for water exchange on divalent octahedral metal-ions going from manganese(II) to

575   nickel(II). Inorganic Chemistry, 19(12), 3696-3703.

576   Duncan, W.T., Bell, R.L., and Truong, T.N. (1998) TheRate: Program for ab initio direct

577   dynamics calculations of thermal and vibrational-state-selected rate constants. Journal of

578   Computational Chemistry, 19(9), 1039-1052.

579   Feitknecht, W.; Hodler, M. (1969) Hydration of nickle oxide. Zeitschrift Fur Physikalische

580   Chemie-Frankfurt, 64(1-4),141.

581   Foresman, J. B.; Frisch, A. Exploring Chemistry with Electronic Structure Methods, 2nd ed.;

582   Gaussian, Inc.: Pittsburgh, PA, 1996.

583   Frisch, M.J., Trucks, G.W., Schlegel, H.B., Scuseria, G.E., Robb, M.A., Cheeseman, J.R.,

584   Montgomery, J.A., Jr., Vreven, T., Kudin, K.N., Burant, J.C., Millam, J.M., Iyengar, S.S.,

585   Tomasi, J., Barone, V., Mennucci, B., Cossi, M., Scalmani, G., Rega, N., Petersson,

586   G.A., Nakatsuji, H., Hada, M., Ehara, M., Toyota, K., Fukuda, R., Hasegawa, J., Ishida,

587   M., Nakajima, T., Honda, Y., Kitao, O., Nakai, H., Klene, M., Li, X., Knox, J.E.,

588   Hratchian, H.P., Cross, J.B., Bakken, V., Adamo, C., Jaramillo, J., Gomperts, R.,

589   Stratmann, R.E., Yazyev, O., Austin, A.J., Cammi, R., Pomelli, C., Ochterski, J.W.,

590   Ayala, P.Y., Morokuma, K., Voth, G.A., Salvador, P., Dannenberg, J.J., Zakrzewski,

591   V.G., Dapprich, S., Daniels, A.D., Strain, M.C., Farkas, O., Malick, D.K., Rabuck, A.D.,

592   Raghavachari, K., Foresman, J.B., Ortiz, J.V., Cui, Q., Baboul, A.G., Clifford, S.,

593   Cioslowski, J., Stefanov, B.B., Liu, G., Liashenko, A., Piskorz, P., Komaromi, I., Martin,

594   R.L., Fox, D.J., Keith, T., Al-Laham, M.A., Peng, C.Y., Nanayakkara, A., Challacombe,

27

595   M., Gill, P.M.W., Johnson, B., Chen, W., Wong, M.W., Gonzalez, C., and Pople, J.A.

596   (2004) Gaussian03, Revision E.01. Gaussian, Inc., Wallingford, CT.

597   Furrer, G., and Stumm, W. (1986) The coordination chemistry of weathering .1. dissolution

598   kinetics of delta-Al_2O_3 and BeO. Geochimica et Cosmochimica Acta, 50(9), 1847-1860.

599   Helm, L., and Merbach, A.E. (1999) Water exchange on metal ions: experiments and

600   simulations. Coordination Chemistry Reviews, 187(1), 151-181.

601   -. (2002) Applications of advanced experimental techniques: high pressure NMR and computer

602   simulations. Journal of the Chemical Society-Dalton Transactions, 633-641.

603   -. (2005) Inorganic and bioinorganic solvent exchange mechanisms. Chemical Reviews, 105(6),

604   1923-1959.

605   Ikeda, T., Boero, M., and Terakura, K. (2007) Hydration properties of magnesium and calcium

606   ions from constrained first principles molecular dynamics. Journal of Chemical Physics,

607   127(7), 074503.

608   Jalilehvand, F., Spangberg, D., Lindqvist-Reis, P., Hermansson, K., Persson, I., and Sandstrom,

609   M. (2001) Hydration of the calcium ion. An EXAFS, large-angle X-ray scattering, and

610   molecular dynamics simulation study. Journal of the American Chemical Society, 123(3),

611   431-441.

612   Kang, S.K., Lam, B., Albright, T.A., and O'Brien, J.F. (1991) The water exchange-reaction for

613        $M(H_2O)_6^{2+}$ systems. New Journal of Chemistry, 15(10-11), 757-762.

614   Langford, C.H., and Gray, H.B. (1966) Ligand Substitution Processes. W. A. Benjamin, Inc.,

615   New York.

616   Lee, C., Yang, W., and Parr, R.G. (1988) Development of the Colle-Salvetti correlation-energy

617   formula into a functional of the electron density. Physical Review B, 37(2), 785-789.

28

618 Liu, Y., Olsen, A.A., and Rimstidt, J.D. (2006) Mechanism for the dissolution of olivine series
619   minerals in acidic solutions. American Mineralogist, 91(2-3), 455-458.

620 Ludwig, C., Casey, W.H., and Rock, P.A. (1995) Prediction of ligand-promoted dissolution rates
621   from the reactivities of aqueous complexes. Nature, 375(6526), 44-47.

622 Morrow, C.P., Kubicki, J.D., Mueller, K.T., and Cole, D.R. (2010) Description of Mg^{2+} release
623   from forsterite using ab initio methods. Journal of Physical Chemistry C, 114(12), 5417-
624   5428.

625 Morrow, C.P., Nangia, S., and Garrison, B.J. (2009) Ab initio investigation of dissolution
626   mechanisms in aluminosilicate minerals. Journal of Physical Chemistry A, 113(7), 1343-
627   1352.

628 Nangia, S., and Garrison, B.J. (2008) Reaction rates and dissolution mechanisms of quartz as a
629   function of pH. Journal of Physical Chemistry A, 112(10), 2027-2033.

630 -. (2009) Ab initio study of dissolution and precipitation reactions from the edge, kink, and
631   terrace sites of quartz as a function of pH. Molecular Physics, 107(8-12), 831-843.

632 Neely, J., and Connick, R. (1970) Rate of water exchange from hydrated magnesium ion. Journal
633   of the American Chemical Society, 92(11), 3476-3478.

634 Pokrovsky, O.S., and Schott, J. (2000) Forsterite surface composition in aqueous solutions: A
635   combined potentiometric, electrokinetic, and spectroscopic approach. Geochimica et
636   Cosmochimica Acta, 64(19), 3299-3312.

637 Richens, D.T. (2005) Ligand substitution reactions at inorganic centers. Chemical Reviews,
638   105(6), 1961-2002.

639 Rosso, J.J., and Rimstidt, J.D. (2000) A high resolution study of forsterite dissolution rates.
640   Geochimica et Cosmochimica Acta, 64(5), 797-811.

29

641   Rotzinger, F.P. (1996) Structure of the transition states and intermediates formed in the water-

642   exchange of metal hexaaqua ions of the first transition series. Journal of the American

643   Chemical Society, 118(28), 6760-6766.

644   -. (1997) Mechanism of water exchange for the di- and trivalent metal hexaaqua ions of the first

645   transition series. Journal of the American Chemical Society, 119(22), 5230-5238.

646   -. (2005a) Performance of molecular orbital methods and density functional theory in the

647   computation of geometries and energies of metal aqua ions. Journal of Physical

648   Chemistry B, 109(4), 1510-1527.

649   -. (2005b) Treatment of substitution and rearrangement mechanisms of transition metal

650   complexes with quantum chemical methods. Chemical Reviews, 105(6), 2003-2037.

651   Schwenk, C.F., Loeffler, H.H., and Rode, B.M. (2001) Molecular dynamics simulations of Ca^{2+}

652   in water: Comparison of a classical simulation including three-body corrections and

653   Born-Oppenheimer   ab   initio   and   density   functional   theory   quantum

654   mechanical/molecular mechanics simulations. Journal of Chemical Physics, 115(23),

655   10808-10813.

656   Sousa, S.F., Fernandes, P.A., and Ramos, M.J. (2007) General performance of density

657   functionals. Journal of Physical Chemistry A, 111(42), 10439-10452.

658   Stumm, W., and Wollast, R. (1990) Coordination chemistry of weathering - Kinetics of the

659   surface-controlled dissolution of oxide minerals. Reviews of Geophysics, 28(1), 53-69.

660   TheRate. (2006). The CSE-Online Project, University of Utah.

661   Tsutsui, Y., Wasada, H., and Funahashi, S. (1997) Theoretical study of water-exchange reactions

662   of hexahydrated divalent cations in the first transition series: relationship between

30

663   reaction mechanism and stability of heptacoordinated species. Bulletin of the Chemical

664   Society of Japan, 70, 1813-1825.

665 Vosko, S.H., Wilk, L., and Nusair, M. (1980) Accurate spin-dependent electron liquid

666   correlation energies for local spin density calculations: a critical analysis. Canadian

667   Journal of Physics, 58, 1200-1211.

668 Wang, J.W., Rustad, J.R., and Casey, W.H. (2007) Calculation of water-exchange rates on

669   aqueous polynuclear clusters and at oxide-water interfaces. Inorganic Chemistry, 46(8),

670   2962-2964.

671 Westrich, H.R., Cygan, R.T., Casey, W.H., Zemitis, C., and Arnold, G.W. (1993) The

672   dissolution kinetics of mixed-cation orthosilicate minerals. American Journal of Science,

673   293(9), 869-893.

674 Xiao, Y., and Lasaga, A.C. (1994) Ab initio quantum mechanical studies of the kinetics and

675   mechanisms of silicate dissolution: $H+(H_3O)^+$ catalysis. Geochimica et Cosmochimica

676   Acta, 58(24), 5379-5400.

677 -. (1996) Ab initio quantum mechanical studies of the kinetics and mechanisms of quartz

678   dissolution: OH^- catalysis. Geochimica et Cosmochimica Acta, 60(13), 2283-2295.

679

680

681

682

683

31

List of Figure Captions

Figure 1. (a) The potential energy surface (PES) scan (blue line with blue squares) and optimized energy profile (red line with red squares) for hydrolysis of a protonated Ni–O–Si site where energy (kJ/mol) is plotted versus reaction coordinate. (b) The reaction mechanism for this reaction where the reactant complex (RC), transition state (TS), and product complex (PC) are presented. The nickel ion is blue, silicon atom turquoise, oxygen atoms red, and hydrogen atoms white.

Figure 2. (a) The PES scan (black line with open diamonds) and optimized energy profile (green line with closed diamonds) for H_2O exchange around Mg in a protonated Mg–O–Si site where energy (kJ/mol) is plotted versus reaction coordinate. (b) The reaction mechanism for this reaction where the RC, TS, and PC are presented. The magnesium ion is yellow, silicon atom turquoise, oxygen atoms red, and hydrogen atoms white. The green and blue circles represent H_2O molecules originally in the first and second hydration spheres, respectively.

Figure 3. (a) The PES scan (blue line with blue diamonds) and optimized energy profile (red line with red diamonds) for hydrolysis of a protonated Mg–O–Si site where energy (kJ/mol) is plotted versus reaction coordinate. (b) The reaction mechanism for this reaction where the RC, TS, and PC are presented. The color scheme is the same as for Figure 2.

Figure 4. (a) The PES scan (black line with open triangles) and optimized energy profile (green line with closed triangles) for H_2O exchange around Ca^{2+} in a protonated Ca–O–Si site where energy (kJ/mol) is plotted versus reaction coordinate. (b) The reaction mechanism for this reaction where the RC, TS, and PC are presented. The calcium ion is gold, silicon atom turquoise, oxygen atoms red, and hydrogen atoms white.

32

709

710   **Figure 5.** (a) The PES scan for the forward direction (blue line with closed triangles), the PES scan for

711   the reverse direction (open blue triangles), and optimized energy profile (red line with closed triangles)

712   for hydrolysis of a protonated Ca–O–Si site where energy (kJ/mol) is plotted versus reaction coordinate.

713   (b) The reaction mechanism for this reaction where the RC, TS, and PC are presented. The color scheme

714   is the same as for Figure 4.

715

716   **Figure 6.** The log of the rate constant k (s^{-1}) for hydrolysis and H_2O exchange at protonated Ni–O–Si,

717   Mg–O–Si, and Ca–O–Si sites (from this work) versus the log of the rate constant k (s^{-1}) of H_2O exchange

718   for each of the corresponding metal ions (Casey and Westrich, 1992; Helm and Merbach, 1999).

719

720

33

721 **Table 1:** Relevant distances (Å) and bond angles (°) in the reactions for protonated Ni–O–Si, Mg–O–Si, and Ca–O–Si sites.

Reaction Type	Optimized Structure	Forming Bond (Å)	Breaking Bond (Å)	Angle Type	Bond Angles (deg)
		Ni–O–Si			
H$_2$O Exchange/ Hydrolysis					
		Ni–H$_2$O$_{2nd}$	Ni–O		
	RC	3.81	2.10		
	TS	2.51	2.14	O–Ni–H$_2$O$_{eq}$	109, 109, 83, 83
				H$_2$O$_{ax}$–Ni–H$_2$O$_{eq}$	82, 87, 86, 78
	PC	2.11	4.02		
		Mg–O–Si			
H$_2$O Exchange					
		Mg–H$_2$O$_{2nd}$	Mg–H$_2$O$_{1st}$		
	RC	3.85	2.10		
	TS	2.20	2.26		
				O–Mg–H$_2$O$_{eq}$	106, 107, 82, 80
	PC	2.10	3.84	H$_2$O$_{ax}$–Mg–H$_2$O$_{eq}$	77, 83, 89, 85
Hydrolysis					
		Mg–H$_2$O$_{2nd}$	Mg–O		
	RC	3.85	2.14		
	TS	4.28	3.74	O–Mg–H$_2$O$_{eq}$	70, 105, 72, 70
				H$_2$O$_{ax}$–Mg–H$_2$O$_{eq}$	112, 91, 109, 93
	PC	2.09	4.11		
		Ca–O–Si			
Hepta-coordinated Ca^{2+}					
		Ca–H$_2$O$_{2nd}$	Ca–O		
	RC	4.09	2.46		
	TS	2.99	2.45	O–Ca–H$_2$O$_{eq}$	122, 100, 75, 77
				H$_2$O$_{ax}$–Ca–H$_2$O$_{eq}$	84, 93, 84, 77
	PC	2.51	2.52		
Hydrolysis					
		Ca–H$_2$O$_{2nd}$	Ca–O		
	RC	4.09	2.46		
	TS	2.44	3.04	O–Ni–H$_2$O$_{eq}$	83, 92, 79, 87
				H$_2$O$_{ax}$–Ni–H$_2$O$_{eq}$	124, 93, 75, 92

34

PC   2.39   4.34

35

722   **Table 2:** Barrier heights (kJ/mol) for H_2O exchange and hydrolysis of protonated Ni–O–Si, Mg–O–Si,

723   and Ca–O–Si sites.

Reaction Type	Barrier Height (kJ/mol)
Ni–O–Si	
H_2O Exchange/Hydrolysis	76
Mg–O–Si	
H_2O Exchange	69
Hydrolysis	54
Ca–O–Si	
Hepta-Coordinated Ca^{2+}	24
Hydrolysis	27

724

725

726

727

36

728   **Table 3:** Pre-exponential factors A (s^{-1}) and rate constants k (s^{-1}) for H_2O exchange and hydrolysis of

729   protonated Ni–O–Si, Mg–O–Si, and Ca–O–Si sites.

Reaction Type	A (s^{-1})	k (s^{-1})
Ni–O–Si		
H_2O Exchange/Hydrolysis	1.7×10^{13}	7.2×10^{-1}
Mg–O–Si		
H_2O Exchange	3.1×10^{13}	2.6×10^{1}
Hydrolysis	1.4×10^{14}	4.7×10^{4}
Ca–O–Si		
Hepta-Coordinated Ca^{2+}	4.9×10^{13}	3.7×10^{9}
Hydrolysis	9.3×10^{13}	1.5×10^{9}

730

37

731   **Figure 1.** (a) The potential energy surface (PES) scan (blue line with blue squares) and optimized energy

732   profile (red line with red squares) for hydrolysis of a protonated Ni–O–Si site where energy (kJ/mol) is

733   plotted versus reaction coordinate. (b) The reaction mechanism for this reaction where the reactant

734   complex (RC), transition state (TS), and product complex (PC) are presented. The nickel ion is blue,

735   silicon atom turquoise, oxygen atoms red, and hydrogen atoms white.

736   (a)

748

(b)

38
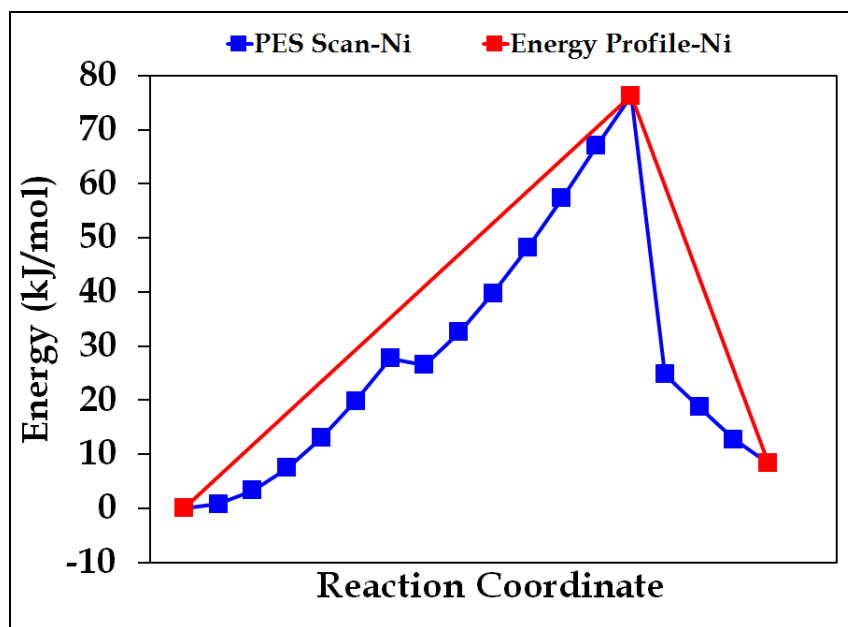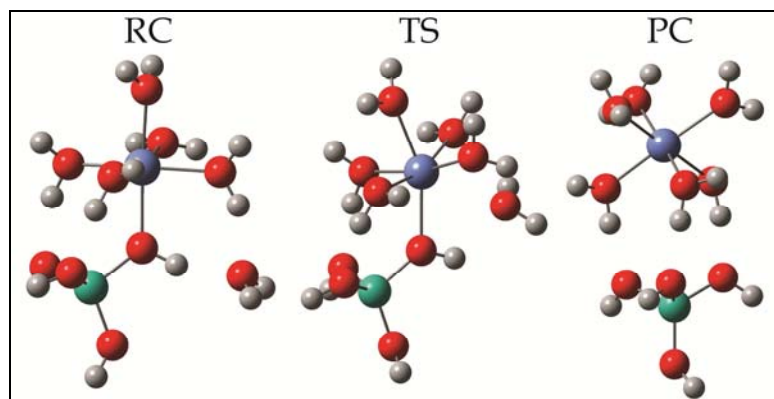
749   **Figure 2.** (a) The PES scan (black line with open diamonds) and optimized energy profile (green line

750   with closed diamonds) for H_2O exchange around Mg in a protonated Mg–O–Si site where energy

751   (kJ/mol) is plotted versus reaction coordinate. (b) The reaction mechanism for this reaction where the RC,

752   TS, and PC are presented. The magnesium ion is yellow, silicon atom turquoise, oxygen atoms red, and

753   hydrogen atoms white. The green and blue circles represent H_2O molecules originally in the first and

754   second hydration spheres, respectively.

755

756   (a)

757

768   (b)

769
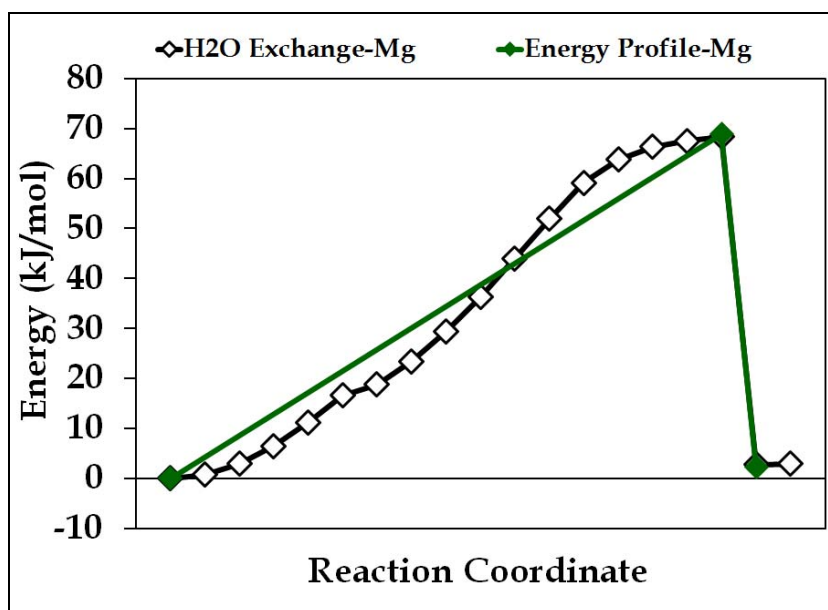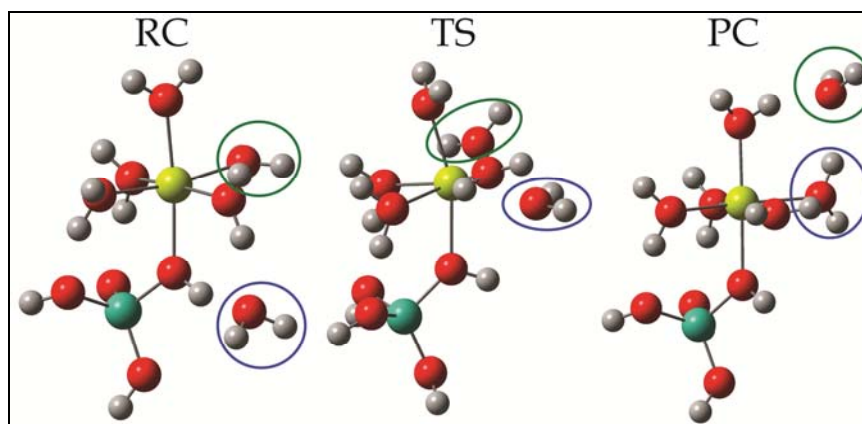
39

772   **Figure 3.** (a) The PES scan (blue line with blue diamonds) and optimized energy profile (red line with red

773   diamonds) for hydrolysis of a protonated Mg–O–Si site where energy (kJ/mol) is plotted versus reaction

774   coordinate. (b) The reaction mechanism for this reaction where the RC, TS, and PC are presented. The

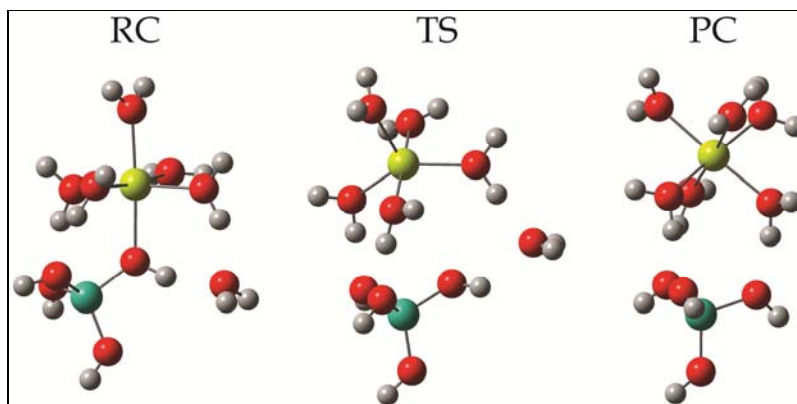775   color scheme is the same as for Figure 2.

776

777   (a)

778
779
780
781
782
783
784
785
786
787
788

789

790   (b)

791
792
793
794
795
796
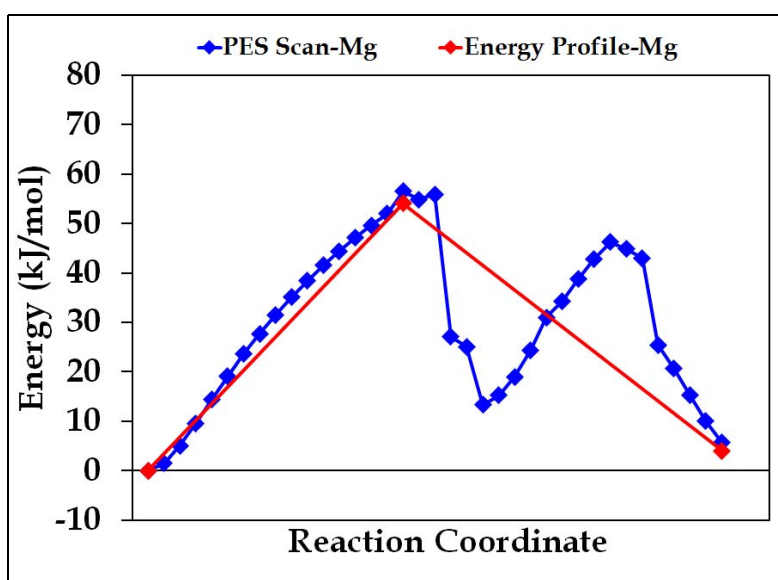
40

797   **Figure 4.** (a) The PES scan (black line with open triangles) and optimized energy profile (green line with

798   closed triangles) for H_2O exchange around Ca^{2+} in a protonated Ca–O–Si site where energy (kJ/mol) is

799   plotted versus reaction coordinate. (b) The reaction mechanism for this reaction where the RC, TS, and

800   PC are presented. The calcium ion is gold, silicon atom turquoise, oxygen atoms red, and hydrogen atoms
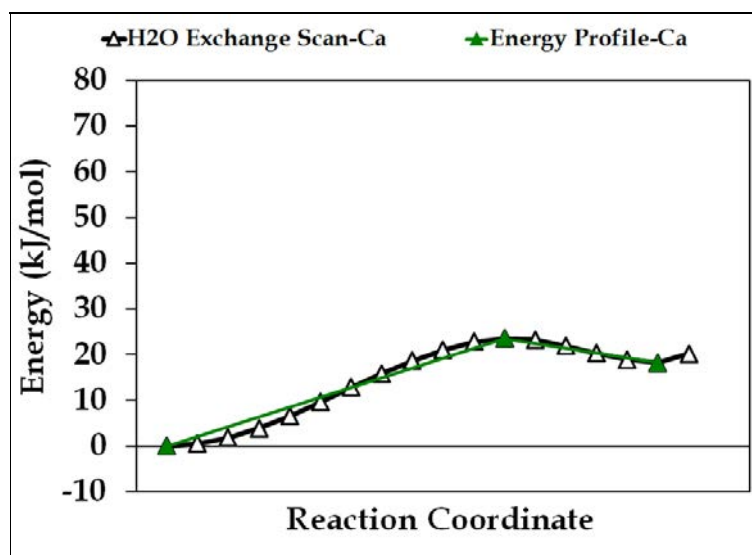
801   white.

802

(a)

803

804

805

806

807

808

809

810

811

812

813

814

(b)

815

816

817

818

819

820
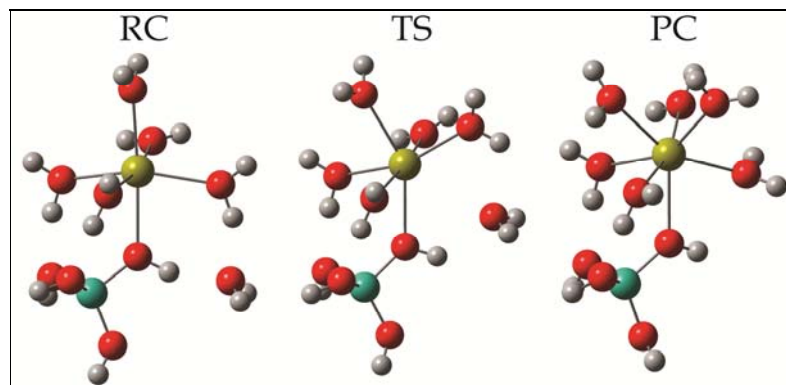
41

821   **Figure 5.** (a) The PES scan for the forward direction (blue line with closed triangles), the PES scan for

822   the reverse direction (open blue triangles), and optimized energy profile (red line with closed triangles)

823   for hydrolysis of a protonated Ca–O–Si site where energy (kJ/mol) is plotted versus reaction coordinate.

824   (b) The reaction mechanism for this reaction where the RC, TS, and PC are presented. The color scheme

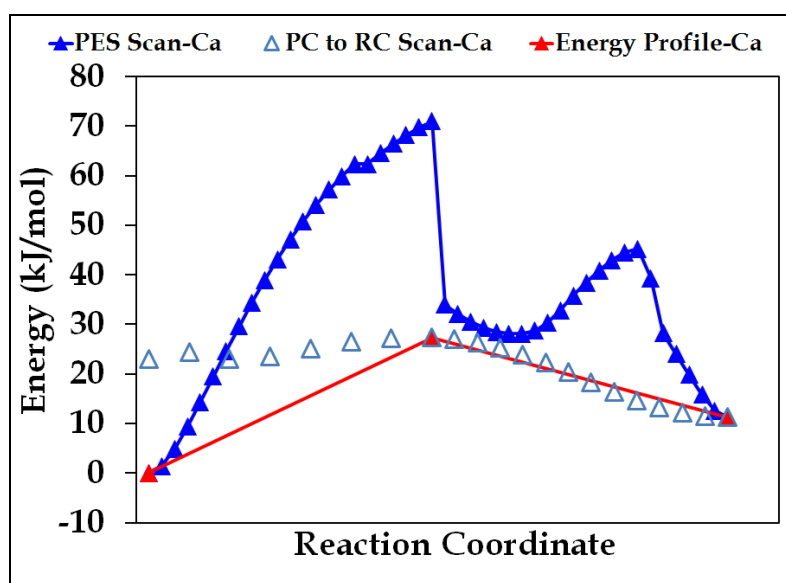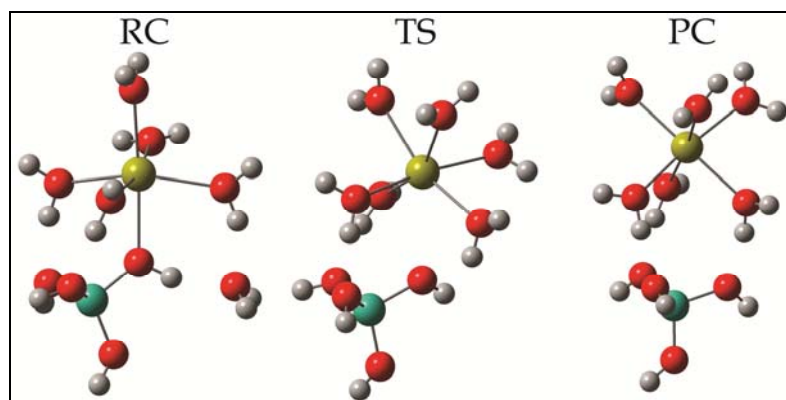825   is the same as for Figure 4.

826

(a)
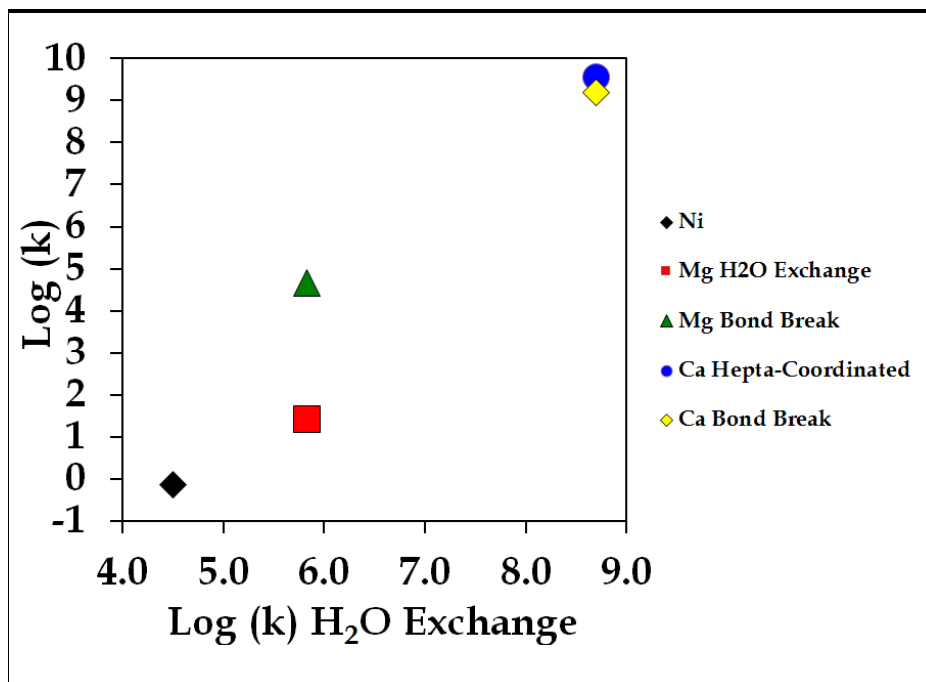
827

828

839

(b)

840

42

841 **Figure 6.** The log of the rate constant k (s^{-1}) for hydrolysis and H_2O exchange at protonated Ni–O–Si,

842 Mg–O–Si, and Ca–O–Si sites (from this work) versus the log of the rate constant k (s^{-1}) of H_2O exchange

843 for each of the corresponding metal ions (Casey and Westrich, 1992; Helm and Merbach, 1999).

844

845

846

847

848

43